Physica Medica 68 (2019) 1–9

Contents lists available at ScienceDirect

Physica Medica

journal homepage: www.elsevier.com/locate/ejmp

Original paper

Measuring radioenhancement by gold nanofilms: Comparison with analytical calculations

Jamal Ahmad Mirza[a,b,1], Kwon Choi[a,1], Wonmo Sung[a], Seongmoon Jung[a], Sung-Joon Ye[a,c,d,*]

[a] Program in Biomedical Radiation Sciences, Department of Transdisciplinary Studies, Graduate School of Convergence Science and Technology, Seoul National University, Seoul 08826, South Korea
[b] Isotope Production Division, Pakistan Institute of Nuclear Science and Technology, Nilore, Islamabad 44000, Pakistan
[c] Biomedical Research Institute, Seoul National University Hospital, Seoul 03080, South Korea
[d] Robotics Research Laboratory for Extreme Environments, Advance Institutes of Convergence Technology, Seoul National University, Suwon 16229, South Korea

ARTICLE INFO

Keywords:
Gold nanoparticle and nanofilm
Radioenhancement
Radiochromic film
Optical scanner
Raman spectrometer

ABSTRACT

Purpose: To measure radioenhancement by gold nanoparticles (GNPs) using gold nanofilms (GNFs).
Methods: GNFs of 20–100 nm thicknesses were prepared. The GNF attached to radiochromic film (RCF) was irradiated using 50, 220 kVp, and 6 MV X-rays. The radiation doses to the active layer of RCF with and without GNF were measured using an optical flatbed scanner and Raman spectrometer to estimate the dose enhancement factor (DEF). For verification, analytical calculations of DEF within the thickness of active layer and the ranges of secondary electrons were carried out.
Results: The DEFs for GNFs of 20 to 100 nm thicknesses measured by an optical scanner ranged from 2.1 to 6.1 at 50 kVp and 1.6 to 4.9 at 220 kVp. Similarly, the DEFs measured by Raman spectroscopy ranged from 2.6 to 4.6 at 50 kVp and 2.2 to 4.8 at 220 kVp. The calculated DEFs ranged from 1.5 to 3.6 at 50 kVp and from 1.7 to 4.7 at 220 kVp. Almost no dose enhancement was observed in 6 MV X-ray. The analytical DEFs seemed to be underestimated by averaging local enhancement over the entire active layer. However, analytical DEFs within the ranges of secondary electrons was much higher than the measured macroscopic DEFs.
Conclusions: The experimental and analytical approaches developed in this study could quantitatively estimate radioenhancement by GNPs. Due to a short range of low-energy electrons emitted from gold, the microscopic radioenhancement within the ranges of low-energy electrons would be particularly important in a cell.

1. Introduction

The advent of nanotechnology has given a new dimension to the diagnostic and therapeutic management of cancer [1–5]. Promising results from early *in vivo* and *in vitro* experiments confirmed that the metal nanoparticles (NPs) have great potential to maximize the therapeutic effect of radiotherapy [6–13]. The so called "radioenhancement" can be explained by the phenomenon that low-energy photons (below a hundred keV) have large peak cross-sections of photoelectric interaction on K- and L-shells of high-Z materials (e.g., ^{79}Au-/^{64}Gd-NPs). Atomic reorganization after these photoelectric interactions leads to the emission of a large number of low-energy electrons (LEE) i.e., photoelectrons (PE), Auger electrons (AE) and Coster-Kronig electrons [14]. Assuming loading of metal NPs to tumors, these LEEs following the photoelectric interactions penetrate into the surrounding tumorous tissue and result in a significantly increased energy deposition within a few tens nanometer range from the metal NPs [14,15]. Previous studies have shown that an existence of ^{79}Au-/^{64}Gd-NPs near the tumor, increases the cell-killing when exposed to low-energy photons [11,12,14]. The mechanism of this efficient cell-killing is still unclear; however possible reasons may include macro- and micro-scale dose enhancement explained above, generation of reactive oxygen species, cell cycle effects, DNA damage, and cytoplasmic events [14]. The main source for the radioenhancement of NPs is abundant LEEs as their relative biological effectiveness is greater than one [15,16].

The dose enhancement factor (DEF) of metal NPs is defined as the ratio of a dose in the presence of metal NPs to that without metal NPs [15]. Earlier studies using biological *in vitro* and animal models examined the macroscopic dose enhancement by metal NPs [17]. Rakowski *et al.* recently combined experimental results of EBT2 Gafchromic™ film and Monte Carlo (MC) modeling and found a DEF of

* Corresponding author at: Seoul National University Hospital, 101 Daehangro, Jongno-Gu, Seoul 03080, South Korea.
E-mail address: sye@snu.ac.kr (S.-J. Ye).
[1] Jamal Ahmad Mirza and Kwon Choi contributed equally to this work.

https://doi.org/10.1016/j.ejmp.2019.10.040
Received 24 May 2019; Received in revised form 18 October 2019; Accepted 29 October 2019
Available online 09 November 2019

18.31 within the first 0.25 μm water depth from 23.1 nm-thick gold nanofilm (GNF) [15]. More recent studies considered microscopic dose distributions and used microscopic DEFs to predict cell survival for various ionizing radiation beams [11,18–20]. Experimental quantification of microscopic DEF in the immediate vicinity of metal NPs has been limited due to nanoscale ranges of LEEs. Therefore, MC simulations have been most widely used to predict microscopic DEFs [17].

The purpose of this study is to experimentally measure the macroscopic DEF of GNFs for low- and high-energy X-rays by using a technique similar to Rakowski *et al.*; however, the dosimeter and detectors used in this study were different from the previous study. Various thicknesses of GNFs and a wide range of X-ray energies were investigated in this study. The experimental results were then verified by analytical calculations. Radioenhancements from the NPs were first analytically calculated by Roeske *et al.* [21]. However, in this study, the concept of microscopic radioenhancement within the ranges of electrons was defined and analytically calculated. The advantage of using GNFs over gold nanoparticles (GNPs) was to measure a volume-averaged dose rather than a point dose. GNFs with the thickness equivalent to the size of GNPs were expected to show similar interactions with ionizing radiation especially when GNPs aggregate in the proximity of tumor vasculature or tumor cell membrane.

2. Materials and methods

2.1. Preparation of GNF

A 188 μm-thick polyethylene terephthalate (PET) film was cut into $1 \times 1\ cm^2$ pieces as coating substrates for GNFs. The PET substrates were rinsed with distilled water after washing in an ultrasonic cleaner with ethanol as a cleaning solvent. GNFs were prepared using a thermal evaporation technique. The gold was heated and vaporized under vacuum condition in a thermal evaporator (Centus OL100). The evaporated gold particles moved up and deposited on the PET substrate to form a thin layer of gold. GNFs with nominal thicknesses of 20, 30, 40, 50, and 100 nm were prepared by adjusting the deposition time.

The actual thicknesses of deposited gold layer on PET substrates were measured with Alpha-Step profiler (Alpha-Step IQ surface profiler, KLA Tencor) [22]. Alpha-Step is a stylus-based surface profiler, which can scan the surface status of a sample. Slits were made at three randomly selected areas of each nanofilm sample. The depth from the surface of GNF to the surface of substrate at a slit was measured as the thickness of GNF. The depth of each slit was measured 10 times and averaged using a step analysis mode with multi-scans. The scan speed was 20 μm/s with a sampling rate of 100 Hz. The estimated gold-thicknesses were used in the MC simulations.

2.2. Preparation of RCF samples

EBT-XD radiochromic film (RCF) type (Ashland Specialty Ingredients, Bridge Water, NJ, USA) is a suitable radiochromic dosimeter due to its high spatial resolution, near-tissue equivalence, energy independence and dose-rate independence, and can be readout using an optical flatbed scanner, a microdensitometer, and a Raman microspectrometer [23–26]. At kVp X-rays energy ranges, previous RCF models such as EBT2 showed strong energy dependence due to the increased cross-sections of photoelectric interactions of high Z elements within the active layer [15]. Use of strong energy dependent RCF may lead to significant over- or under-estimation of DEFs [24]. At MV X-rays energy ranges, the RCFs are almost energy independent. In this study, the EBT-XD films were used to measure the macroscopic DEF caused by photon interactions with GNFs.

The film has an active layer of 25 μm, which is sandwiched between two matte polyester substrates of 125 μm [27,28]. When it is exposed to radiation, it reacts to form a blue colored polymer in its active layer [27]. A matte polyester substrate from one side of the EBT-XD film was carefully removed to avoid the energy loss of incident radiation in this protective layer. This unlaminated EBT-XD film was cut into $3 \times 3\ cm^2$ pieces. A $1 \times 1\ cm^2$ piece of GNF was placed in direct contact with the active layer of the unlaminated EBT-XD film and attached tightly by using an adhesive tape. The orientation of GNF was adjusted so that the coated side of GNF contacted the active layer of the unlaminated EBT-XD film. A piece of PET film (without gold) was placed next to the GNF for comparison (also see Fig. 1). For calibration, pieces of the unlaminated EBT-XD film attached to PET film were also prepared.

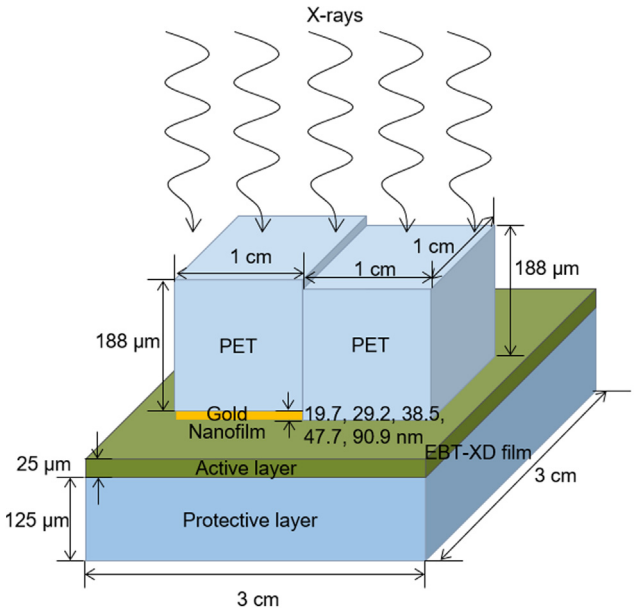

Fig. 1. Schematic of GNF and unlaminated EBT-XD film irradiated by X-rays (not scaled). On the active layer of the unlaminated EBT-XD film, GNF and PET without gold were irradiated by X-ray beams. PET without gold was used as a control to calculate DEF. Beneath this geometry, a 5 cm solid water was placed for backscatter. For 6 MV FFF beam, a 5 cm build-up phantom was additionally placed on the top of this geometry.

2.3. Sample irradiation and calibration

X-ray beams of 50 and 220 kVp, (XRAD 320 Biological Irradiator, Precision X-Ray, Inc., N. Branford, CT) and flattening filter free (FFF) 6 MV (Trilogy Varian Medical System, Palo Alto, CA) were used to deliver 0.3, 0.5, 1.0, and 1.5 Gy to the prepared samples of RCF attached to GNF and PET film. The active layer of the RCF, placed in direct contact with the GNF can absorb the energy of LEEs emitted as a result of the X-ray interactions with GNF [15]. For calibration, the prepared pieces of RCF attached to PET film were irradiated with doses of 0.3, 0.5, 1.0, 1.5, 2.0, 4.0, 6.0, and 8.0 Gy. All the samples of RCF were irradiated in air at 50 cm source-to-surface distance (SSD) for 50 and 220 kVp beams and at 5 cm depth in solid water at 100 cm source-to-axis distance (SAD) for 6 MV FFF with a field size of $10 \times 10\ cm^2$ (Fig. 1).

2.4. Radiochromic film reading

The GNF and PET film were removed from the unlaminated EBT-XD film once exposed to the X-ray beams. These unlaminated RCFs were then readout by using an optical flatbed scanner and a confocal Raman spectrometer.

2.4.1. Optical flatbed scanner

The RCFs were scanned using a flatbed scanner (Expression 11000XL Epson, Tokyo, Japan). The scanner was operated in the transmission mode at 1200 dpi and 48 bits red–greenblue channels. The scanned images were saved in TIFF format. The central region of the

scanner was used during film scan to evade the lateral response artifact [29,30]. ImageJ v1.51n software (National Institutes of Health, Bethesda, MD, USA) was used to obtain the optical densities from the scanned images [31]. The red channel was adopted due to its better sensitivity and stability over the other channels.

For each of unlaminated EBT-XD films, a mean value of scanner response was obtained from five separated regions of $2 \times 2\,mm^2$ area in the film. Since removing the polyester substrate from one side of the EBT-XD film has a negligible effect, the manufacturer's recommended equation can be efficiently used to convert the mean scanner response to a dose [27]:

$$R(D) = a + \frac{b}{D - c} \quad (1)$$

where R(D) was a scanner response from an irradiated film at a dose D, and a, b, c were the equation parameters for fitting. The scanner responses were then plotted against radiation doses to obtain the calibration curve.

2.4.2. Raman spectroscopy

Raman spectroscopy is based on inelastic scattering of a monochromatic excitation source by molecules. It can be used to identify molecules, as each molecule provides a unique "molecular fingerprint" [32]. Historically, Raman spectroscopy is a preferred choice for the analysis of carbon bonds found in many polymer backbones [33]. The active layer of Gafchromic™ film consists of diacetylene monomers in ordered form, which polymerizes on the application of X-rays and progressively darkens with increased exposure [26,34]. On the basis of previous knowledge of Raman spectrum of diacetylene polymer, Callens et al. allocated bands in the spectrum of EBT3 film [34]. Since the active layers of EBT3 and EBT-XD films are almost identical, both have the same spectra. It was observed that C≡C and C=C increase exponentially with increasing the exposure of X-rays [26]. In this work, we studied the variation in spectra of C≡C stretching bands of diacetylene polymer at $2060\,cm^{-1}$, as a function of therapeutic X-ray dosage with a spatial resolution of 10 μm i.e. at a cellular level.

Raman spectra of each film piece were measured by Ramboss-star microscope Raman system (Dongwoo Optron Co. Ltd, Gyeonggi-Do, Korea) with the Raman shift range of $50\,cm^{-1}$ to $4200\,cm^{-1}$. This system was equipped with the Olympus BX53 microscope and BX3-URA illuminator with M Plan APO 100× objective of 0.70 numerical aperture (Mitutoyo Corp., Japan). A He-Ne laser operating at 632.8 nm was used as a source of excitation. Measurements were taken using a 1200 grooves/mm grating with 0.2 sec laser exposure time and repeated ten times for accumulation. A confocal microscope with a 30 μm pinhole was used, which significantly improved the lateral resolution. For a He-Ne laser of 632.8 nm with 100× objective (Numerical Aperture 0.70), the lateral resolution of the confocal micro-Raman spectroscopy system was determined ~0.36 μm [35,36]. The Raman spectroscopy was calibrated with a silicon wafer at $520\,cm^{-1}$ prior to measurements [37]. Spectra of each film were recorded at minimum of 24 h post-irradiation. Data acquisition and processing were done using Andor SOLIS 4.16.30002.0 (Andor, United Kingdom) and Ramboss mapping 1.02 (DongWoo Optron, Gyeonggi-Do, Korea), respectively. Spectra at different points on RCF were acquired by placing the film on the Märzhäuser motorized XY mapping stage (Märzhäuser Wetzlar GmbH & Co. KG, Germany) with an electrically powered Z-axis focus (minimum step size of stage was 0.05 μm).

The previously developed Raman mapping technique was used to map a region of interest (ROI) of $100 \times 100\,\mu m^2$ on each film with a spatial resolution of 10 μm (scanning time was ~100 sec) [26]. A spatial resolution of 10 μm was chosen to observe the radioenhancement by GNF at a cellular level. Through this, spectra of 121 pixel points per ROI were obtained. The C≡C peaks of each pixel point were preprocessed, which included band selection, smoothing and baseline removal [38]. Thereafter the subtracted peak was fitted with the Lorentzian peak function. The band heights (i.e., Raman intensity values at the peak of Lorentzian distribution) corresponding to 121 points on each film were averaged and the averaged values were plotted as a function of dose to draw the calibration curve.

2.4.3. Microscopic dose enhancement factor

In order to estimate the microscopic dose enhancement on the vicinity of GNP, nano or micrometer scale dosimetry is required. There are no such devices available for this purpose, except for MC simulation. The dosimetry proposed in this study using RCF was actually macroscopic dose estimation that measured an averaged dose on a relatively wide region of interest. A macroscopic DEF is defined as a ratio of the dose deposited in RCF with GNF divided by the dose deposited in the RCF without GNF (i.e. PET only)):

$$MacroscopicDEF = \frac{D_{RCF/GNF}}{D_{RCF}} \quad (2)$$

where $D_{RCF/GNF}$ is the averaged value of estimated doses measured from regions of RCF exposed under GNF and D_{RCF} is that exposed under PET film only.

2.5. Analytical approach

2.5.1. Analytical macroscopic dose enhancement factor

A $10 \times 10\,\mu m^2$ GNF with variable thicknesses (t_{GNF} = 19.7, 29.2, 38.5, 47.7 and 90.9 nm) was placed at the top of the active layer shown in Fig. 2. An X-ray dose (D_{RCF} = 1 Gy) was taken as the dose absorbed by ROI without GNF. The incident photon fluence Φ (cm^{-2}) that corresponds to D_{RCF} was determined to calculate the photoelectron fluence and the radioenhancement by applying the techniques presented in the literature [39–42]. The collisional kerma for a photon beam of energy E (keV) that irradiates a medium of the atomic number Z is related to the energy fluence Ψ (keV/cm^2) by the mass energy absorption coefficient $(\mu_{en}/\rho)_{E,Z}(cm^2/g)$. Under the charged particle equilibrium (CPE) condition, the absorbed dose D (Gy) is equal to the collisional kerma. Therefore, an absorbed dose to the medium is [39]:

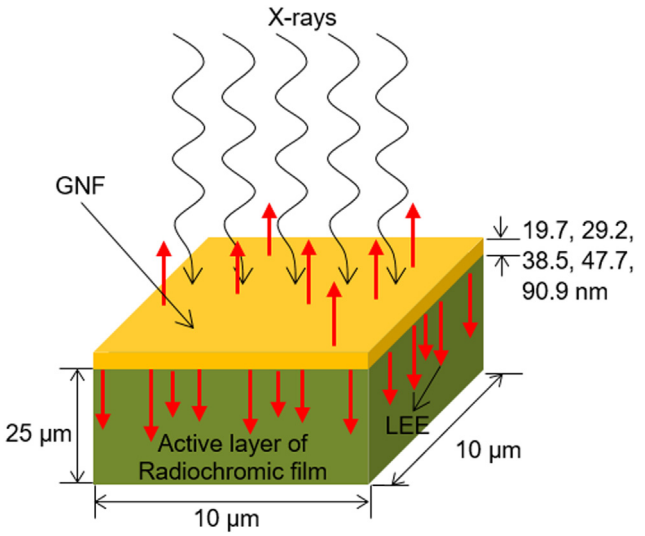

Fig. 2. Schematic diagram of irradiation configurations for analytical calculation of dose enhancement (not scaled). The gold nanofilm (GNF) is attached to the active layer of radiochromic film. A portion of the low-energy electrons (LEE) produced by X-rays will be emitted in the backward direction. The polyester base of radiochromic film and polyethylene terephthalate (PET) substrate of GNF is not shown in the figure.

Table 1
Density and fractional weight composition of PET and EBT-XD films [28].

	Density (g/cm^3)	Fractional composition by weight								
		H	Li	C	N	O	S	Na	Cl	Al
PET	1.38	0.042		0.625		0.333				
Active layer	1.35	0.089	0.006	0.532	0.009	0.291	0.005	0.004	0.006	0.059
Protective layer	1.35	0.042		0.625		0.333				

$$D = 1.602 \times 10^{-13}\left[\frac{Gy}{keV/g}\right] \times \Phi\left[\frac{1}{cm^2}\right] \times E\,[keV] \times \left(\frac{\mu_{en}}{\rho}\right)_{E,Z}\left[\frac{cm^2}{g}\right] \tag{3}$$

where $\Psi = \Phi$. E and Φ is the photon fluence and E is the effective energy of X-rays. For simplicity, the effective energies of 50 and 220 kVp and 6 MV FFF polyenergetic photon beams were set equal to the energy of a monoenergetic X-ray beam that is attenuated at the same rate as the polyenergetic beam. The effective energies of 50 and 220 kVp and 6 MV FFF X-rays were determined to be 25.6, 48.3 and 1970 keV, respectively.

In order to estimate the mass energy absorption coefficient of a uniform mixture, RCF (i.e., EBT-XD film), the additivity rule was applied below:

$$\left(\frac{\mu_{en}}{\rho}\right)_{E,RCF} = f_{Z_1}\left(\frac{\mu_{en}}{\rho}\right)_{E,Z_1} + f_{Z_2}\left(\frac{\mu_{en}}{\rho}\right)_{E,Z_2} + \cdots \tag{4}$$

where f_{Z_i} represents the fractional weight compositions of individual elements in the active layer of RCF (Table 1).

The probability P_{PE} of photoelectric interaction of incident X-rays with GNF of thickness t_{GNF} is:

$$P_{PE} = 1 - \exp\left(-\left(\frac{\mu_{pe}}{\rho}\right)_{E,Au}\left[\frac{cm^2}{g}\right] \times \rho_{GNF}\left[\frac{g}{cm^3}\right] \times t_{GNF}\,[cm]\right) \tag{5}$$

where $\left(\frac{\mu_{pe}}{\rho}\right)_E$ is the photoelectric absorption coefficient of gold at energy E, ρ_{GNF} is the density of GNF (see Table 2). The fluence of emitted photoelectrons (PE) is:

$$\Phi_{PE} = \Phi\left[\frac{1}{cm^2}\right] \times P_{PE} \tag{6}$$

where the value of Φ can be calculated from Eq. (3) when $D = D_{RCF}$. If T_i is the kinetic energy of photoelectron emitted from *ith* sub-shell and $E_{bi}$is the binding energy of that shell, then $T_i = E - E_{bi}$ and the average kinetic energy of emitted PE, T_o is given by

$$T_o = \sum_{i=1}^{n} f_i T_i \tag{7}$$

where f_i is the ratio of photoionization cross-section of *ith* sub-shell to the total photoionization cross-section for E and Z and $i = K, L1, L2, L3, M1, \cdots\cdots\cdots, O1$. The photo-ionization cross-sections of sub-shells higher than $O1$ are ignored because of their negligible contribution to the dose. From Eq. (7), the calculated values of T_o for X-rays with E = 25.6, 48.3 and 1970 keV are 15.4, 37.4 and 1901.5 keV, respectively.

Table 2
Coating thicknesses of gold nanofilms (GNFs) measured by Alpha-Step and their respective densities and masses. Fractions of electrons entering into the active layer of radiochromic film from GNF calculated by the MCNP 6.1 code are also included in the table.

Nominal thickness (nm)	Estimated Thickness (nm)	Au density measured by Siegel *et al.* [50], 2011 (g/cm^3)	Fraction of electrons entering into the active layer from GNF		
			50 kVp	220 kVp	6 MV FFF
20	19.7 ± 0.3	16.1	0.54	0.60	0.87
30	29.5 ± 0.7	16.8	0.54	0.60	0.89
40	38.5 ± 0.5	17.4	0.54	0.61	0.90
50	47.7 ± 0.5	17.8	0.54	0.61	0.91
100	90.9 ± 0.4	18.6	0.54	0.61	0.93

The LEEs produced in GNF by photoelectric interactions at a given X-ray energy, being surrounded by their Coulomb electric field, interact with atoms on their tracks. Each LEE loses kinetic energy continuously in a friction-like process, which is commonly modeled using the continuous-slowing-down approximation (CSDA). The CSDA range ($\Re_{CSDA}$) represents the path length an electron would travel before coming to rest, if its energy loss rate along the path were equal to the mean energy loss rate [39]. The mean value of CSDA range with elemental weight percentage of RCF was obtained from:

$$\frac{1}{(\Re_{CSDA})_{T_o,RCF}} = \frac{f_{Z_1}}{(\Re_{CSDA})_{T_o,Z_1}} + \frac{f_{Z_2}}{(\Re_{CSDA})_{T_o,Z_2}} + \cdots \tag{8}$$

where f_{Z_i} represents the fractional weight compositions of individual elements in the active layer of RCF (Table 1).

The CSDA ranges for low-energy X-rays were calculated to see if there is an unirradiated portion of active layer. The CSDA ranges for PEs of kinetic energies 15.4 (50 kVp X-rays) and 37.4 keV (220 kVp X-rays) are 4.0 μm and 19.5 μm, respectively. Therefore, there is a layer of unirradiated material beyond their range in the active layer of RCF (t_{RCF} = 25 μm). Since the CSDA ranges are less than the thickness of the active layer of RCF for both kVp X-rays, the following equation is used to estimate the dose by PEs in the active layer of RCF [39]:

$$D_{PE} = 1.602 \times 10^{-13}\left[\frac{Gy}{keV/g}\right] \times \Phi_{PE}\left[\frac{1}{cm^2}\right] \times \frac{T_o[1 - Y(T_o)]}{\rho t_{RCF}}\left[\frac{keV}{g/cm^2}\right] \tag{9}$$

where $Y(T_o)$, ρ (see Table 1) and t_{RCF} are the radiation yield, density and thickness of active layer of RCF, respectively. Note that $Y(T_o)$ is close to zero for LEEs.

So far we only considered the fraction of incident X-rays energy transferred to the photoelectrons. A part of the remaining X-rays energy or all of it is converted into either Auger electrons or fluorescent X-rays. For incident X-rays energies lying between K- and highest L-edges of gold (E = 25.6 and 48.3 keV in this work), the energy transferred to Auger electrons, T_{AE} per photoelectric effect event is approximately:

$$T_{AE} = E - T_o - P_L Y_L \times \bar{E_L} \tag{10}$$

where P_L is the fraction of all photoelectric interactions that occur in L-shell, Y_L is the fluorescence yield of L-shell, and $\bar{E_L}$ is the average fluorescence energy in L-shell. Note that the fluorescence yields for M− and higher shells were ignored due to their contribution of less than a few % to the total fluorescence energy. The binding energy of L1, E_{bL1} shell can approximate the $\bar{E_L}$. For gold the product $P_L Y_L \times E_{bL1}$ is estimated as 5 keV [39]. The CSDA ranges, $(\Re_{CSDA})_{T_{AE},GNF}$ of Auger electrons in the gold produced by 25.6 and 48.3 keV X-rays were found to be approximately 141 and 173 nm [43]. The Auger electrons generated in GNF gradually lose their kinetic energy via GNF before reaching the active layer of RCF. The residual CSDA range of these Auger electrons on average would be$(\Re_{CSDA})_{T_{AE},GNF} - t_{GNF}/2$. The Auger electrons with

the remaining kinetic energy, T_{ex}corresponding to this residual CSDA range interact with the active layer of RCF. For X-rays energies lying between K- and highest L-edge, the ratios of L-fluorescence X-rays emitted (fluorescence yield) and Auger electrons (Auger yield) per photoelectric event in L shell of gold are approximately $Y_{\mathrm{Fl}} = 0.35$ and $Y_{\mathrm{AE}} = 0.65$, respectively [43]. Therefore, the dose deposited in the active layer of RCF by Auger electrons, $D_{AE}$is given by

$$D_{AE} = 1.602 \times 10^{-13}\left[\frac{Gy}{keV/g}\right] \times Y_{AE} \times \Phi_{PE}\left[\frac{1}{cm^2}\right] \times \frac{T_{ex}}{\rho t_{RCF}}\left[\frac{keV}{g/cm^2}\right] \tag{11}$$

and L-fluorescence X-rays, $D_{Fl}$is approximately given, if all of them escape from GNF and lose their energy in the active layer, by

$$D_{Fl} = 1.602 \times 10^{-13}\left[\frac{Gy}{keV/g}\right] \times Y_{Fl} \times \Phi_{PE}\left[\frac{1}{cm^2}\right] \times (P_L Y_L \times E_{bL1})[keV] \times \left(\frac{\mu_{en}}{\rho}\right)_{P_L Y_L \times E_{bL1}, RCF}\left[\frac{cm^2}{g}\right] \tag{12}$$

However, the fluorescence X-rays are emitted isotropically; we assume that only half of them will move toward the RCF and deposit most of their energy on the active layer of RCF. Since the GNF is attached on the top of the active layer (see Fig. 2), a portion of the secondary electrons produced by X-rays are emitted to the active layer of RCF. MCNP6.1 (Monte Carlo N-Particle Transport Code Version 6.1) was used to calculate the fraction of backward and forward electrons emitted from GNF (see section 2.E.2.) [44,45]. If f_{Fwd} is the fraction of forward electrons emitted from GNF, the total dose on RCF from LEEs and fluorescence X-rays, D_{Au} is given by:

$$D_{Au} = (D_{PE} + D_{AE}) \times f_{Fwd} + 0.5 D_{Fl} \tag{13}$$

In the case of 6 MV FFF X-rays, the CSDA range for PEs of kinetic energy 1901.5 keV is ~6998 μm. Since the CSDA range is significantly larger than the thickness of the active layer of RCF, the collision stopping power is almost constant throughout the active layer. Therefore, for 6 MV FFF X-rays, the following equation is used for the dose to the active layer of RCF by GNF, D_{Au} [39]:

$$D_{Au} = 1.602 \times 10^{-10}\left(\frac{Gy}{MeV/g}\right) \times f_{Fwd} \times \Phi_{PE}\left(\frac{1}{cm^2}\right) \times \left(\frac{dT}{\rho dx}\right)_c \left(\frac{MeVcm^2}{g}\right) \tag{14}$$

where $\left(\frac{dT}{\rho dx}\right)_c$ is the mass collision stopping power. The macroscopic DEF over the active layer of RCF for the real experimental setup using GNF is given by:

$$DEF = \frac{D_{RCF} + D_{Au}}{D_{RCF}} \tag{15}$$

While the photon doses, D_{RCF} and D_{Fl}, were fairly uniform over the entire thickness of active layer of RCF under CPE, the LEE doses, D_{PE} and D_{AE} were limited actually within their ranges in the active layer of RCF. Therefore, *microscopic dose enhancement* only within the range of such LEEs emitted from GNF can be calculated by replacing t_{RCF} in Eqs. (9) and (11) with the range of LEEs, t_{range}.

The mass energy absorption and photoelectric absorption coefficients corresponding to$E$, and stopping powers, CSDA ranges and radiation yields corresponding toT_o were taken from NIST (National Institute of Standards and Technology, US) tables [46,47]. To calculate the average kinetic energy of emitted PEs, the binding energies, and photoelectric cross-sections of sub-shells have been taken from tables provided by GP Williams and JH Scofield, respectively [43,48]. Since the photoelectric cross-sections of sub-shells data were available from 1 to 1500 keV, the extrapolation technique was used to estimate the kinetic energy of PEs generated in GNF by 6 MV FFF X-rays.

2.5.2. Monte Carlo simulations for estimating f_{FWD}

Parallel 25.6, 48.3 and 1970 keV photons were assumed to be incident on GNF in vacuum. The cut-off energy was set to 50 eV for both electron and photon. For the electron and photon transport, a physics library of eprdata12 was used. A single-event electron transport method was applied to LEEs of which energies were lower than 50 keV [49]. F1 tally (surface current) was used to detect the electrons crossing the upper surface (i.e., backward) and the lower surface (i.e., forward) of GNF. The number of particle histories was 5×10^8 for 25.6 and 48.3 keV X-rays and 7.5×10^{10} for 1.97 MeV X-rays. The relative uncertainties (1σ) of the tallies were below 0.86%. The calculated fractions of forward electrons emitted from GNF were inserted into Eqs. (13) and (14) to calculate the dose enhancement in the real experimental condition. In addition, Siegel *et al.* showed that the decline of lattice parameter of gold prepared in the form of a thin layer influences the density of gold [50]. They reported that the gold density increased with increasing the thickness of gold layer and then above 100 nm achieved the bulk value i.e., 19.3 g/cm^3. Their measured densities for the thicknesses of GNF were used to evaluate the mass composition of gold (see below Table 2).

3. Results

3.1. Thickness measurements of GNF

Fig. 3 shows GNFs of nominal thicknesses 20, 30, 40, 50, and 100 nm that were prepared using a thermal evaporator on PET substrates. Coating thicknesses of GNFs were hardly distinguishable by their transparency. The Alpha-Step measured results are presented in Table 2. The thickness of GNF was estimated as a mean value of three different regions of gold slits. All the measured coating thicknesses of GNFs were thinner than the intended (or nominal) values. The deposition thickness depends upon the evaporation time, deposition rate and the type of substrate.

3.2. Calibration curves

The EBT-XD film calibration curves of optical flatbed scanner and Raman spectroscopy for 50 and 220 kVp and 6 MV FFF X-rays are shown in Fig. 4. The scanner responses of films (R) to doses (D) were fitted to Eqs. (16), (17), and (18) using Eq. (1) for the X-rays of three

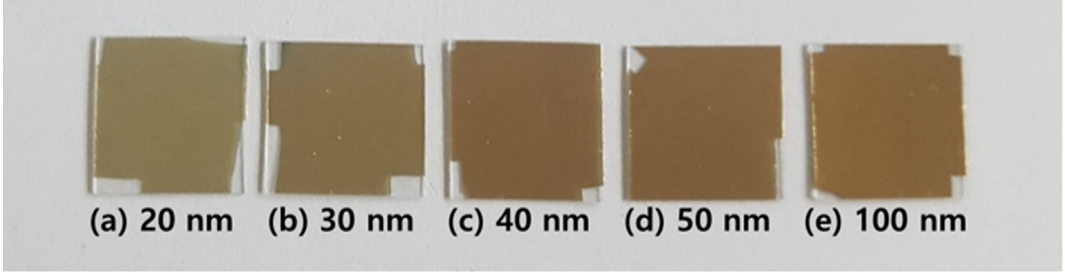

Fig. 3. Gold nanofilms of various coating thicknesses on PET substrate. The thicknesses denoted here are nominal values.

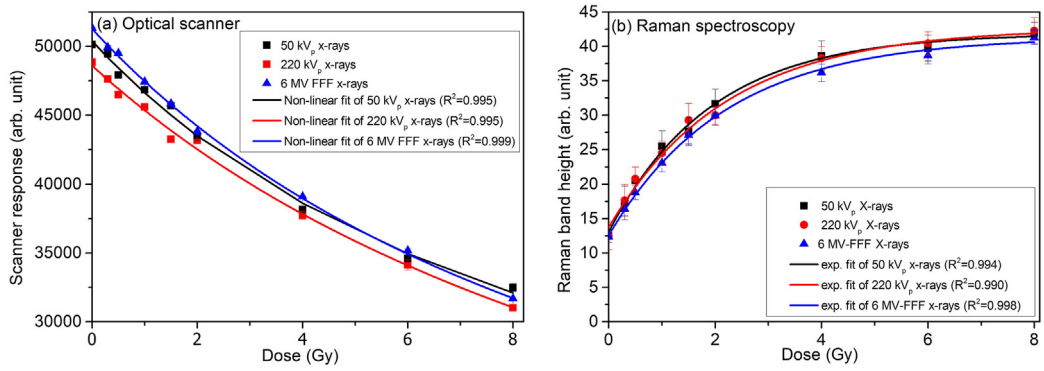

Fig. 4. Dose calibration curves of optical scanner (error bars are the same size or smaller than the symbols) (a) and Raman spectrometer (b) for 50, 220 kVp, and 6 MV FFF.

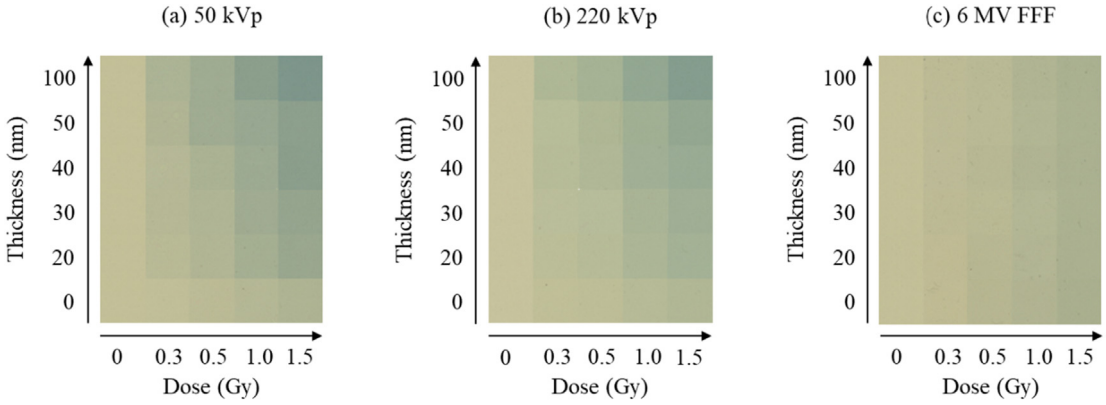

Fig. 5. Arrays of unlaminated EBT-XD films after irradiation of 50, 220 kVp, and 6 MV FFF under GNF. X-axis indicates delivered doses 0 to 1.5 Gy. Y-axis indicates the thicknesses of GNFs 0 to 100 nm. Darker color means that the EBT-XD film was more irradiated (along x-axis) or more dose-enhanced (along y-axis). The color became darker with increasing the thickness of GNF at 50 kVp (a) and 220 kVp beams (b). However, the dose enhancement by change of thickness was hardly seen from the films irradiated by 6 MV FFF beam (c).

Table 3
List of DEFs for 50 and 220 kVp, and 6 MV FFF X-rays for GNFs of various thicknesses. These values were estimated by three different methods i.e. optical scanner, Raman spectrometer and analytical approach with an aid of MC simulations.

GNF Thickness (nm)	50 kVp			220 kVp			6 MV FFF		
	[a]DEF_{OS}	[b]DEF_{RS}	[c]DEF_{AN}	DEF_{OS}	DEF_{RS}	DEF_{AN}	DEF_{OS}	DEF_{RS}	DEF_{AN}
20	2.1 (± 0.3)	2.6 (± 0.6)	1.5	1.6 (± 0.6)	2.2 (± 0.5)	1.7	1.0 (± 0.2)	1.0 (± 0.1)	1.0
30	2.9 (± 0.1)	3.0 (± 0.7)	1.8	2.2 (± 0.4)	2.6 (± 0.6)	2.1	1.0 (± 0.1)	1.0 (± 0.1)	1.0
40	3.6 (± 0.4)	3.6 (± 0.8)	2.1	2.8 (± 0.3)	3.0 (± 0.7)	2.5	1.0 (± 0.0)	1.0 (± 0.1)	1.0
50	3.6 (± 0.3)	3.8 (± 0.9)	2.3	2.8 (± 0.4)	3.6 (± 0.9)	2.9	1.1 (± 0.1)	1.0 (± 0.1)	1.0
100	6.1 (± 0.4)	4.6 (± 1.0)	3.6	4.9 (± 0.4)	4.8 (± 0.8)	4.7	1.0 (± 0.0)	1.0 (± 0.1)	1.0

[a] **DEF_{OS}** measured by optical scanner response
[b] **DEF_{RS}** measured by Raman spectrometer
[c] **DEF_{AN}** Analytical calculations

energies:

$$50kV_p: R(D) = 9641.2 + \frac{400639.8}{D + 9.8} \quad (16)$$

$$220kV_p: R(D) = 1123.1 + \frac{647023.3}{D + 13.6} \quad (17)$$

$$6MVFFF: R(D) = 3576.2 + \frac{546964.5}{D + 11.5} \quad (18)$$

The Raman band height (Y) was exponentially increased with doses (D):

$$50kV_p: Y(D) = 42 - 29e^{-\frac{D}{1.9}} \quad (19)$$

$$220kV_p: Y(D) = 43 - 29e^{-\frac{D}{2.2}} \quad (20)$$

$$6MVFFF: Y(D) = 41 - 29e^{-\frac{D}{2.2}} \quad (21)$$

The dynamic dose range of both methods was well suited within the calibrated range from 0 to 8.0 Gy. In addition, the three energy curves in Fig. 4(a) and (b) are nearly overlapping, showing the weak energy dependence of EBT-XD film. In Fig. 4, the relative standard deviations from the optical scanner and Raman spectrometer were within 1.1% and 10%, respectively.

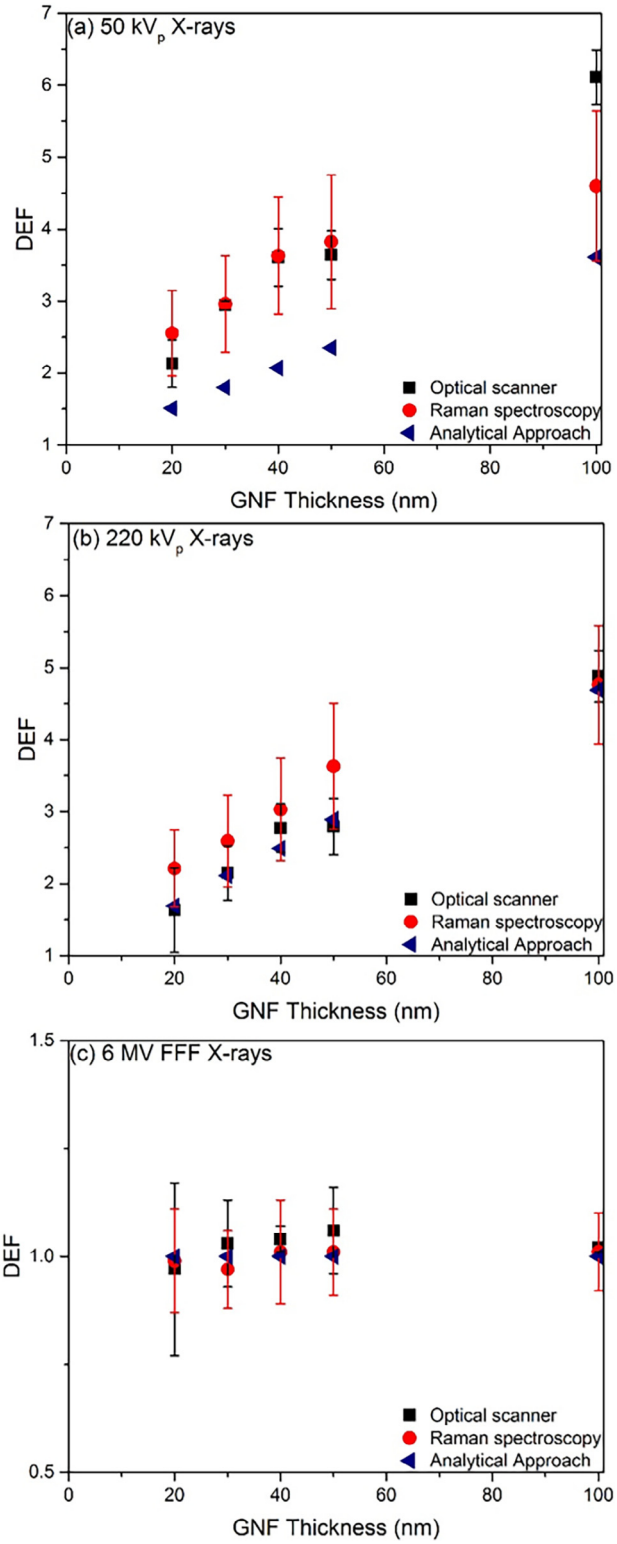

Fig. 6. Comparison of DEF obtained from optical scanner, Raman spectroscopy, and analytical calculations for photon energies of (a) 50 kVp, (b) 220 kVp, and (c) 6 MV FFF beam. For low-energy X-rays DEF was an increasing function of GNF thickness, whereas enhancement was negligible for high-energy X-rays.

3.3. Dose enhancement factor

3.3.1. Experimental measurement

Fig. 5 shows the arrays of EBT-XD films aligned by delivered doses in order and thicknesses of gold-coating. Note that 0 thickness of gold-coating means a PET substrate alone. Fig. 5(a) for 50 kVp and Fig. 5(b) for 220 kVp show that the darkness of EBT-XD films (i.e., optical density) was increased with the thicknesses of gold-coating as well as the doses delivered to the films. However, Fig. 5(c) for 6 MV FFF shows almost no change of the darkness along the y-axis (i.e., regardless of the thickness of gold-coating) and different optical densities developed only by delivered doses (along the x-axis).

The DEFs defined in Eq. (2) were calculated for the three X-ray energies and the five thicknesses of gold-coating from doses estimated by the two measurement methods and the analytical approach. The Chauvenet's criterion was applied to reject outlying data from the measurements [51]. The DEFs determined from this procedure are also summarized in Table 3. Fig. 6 shows variations of DEFs vs. thickness of gold-coating for the three X-ray energies. The fluctuations in measured DEFs were observed in Fig. 6. The non-uniform contact between GNF and the active layer of EBT-XD film at a micro-level might be one of the sources of this variability. In addition, the deviations from a uniform coating were on the order of a micrometer. Since the dose deposited by LEEs reached only a few tens nm depth of the active layer from GNF, such unevenness at the micrometer scale caused a large variation in readouts using both the optical scanner and Raman spectrometer. However, even with this variation, almost all the DEFs measured by the optical scanner lied within the error bars of Raman spectroscopy data.

3.3.2. Analytical approach

Table 2 presents the measured thicknesses of GNFs and their respective gold densities and the fraction of electrons entering into the RCF calculated by MC simulations. Equations (13)–(15) were used to calculate the macroscopic DEFs, which present in Table 3 and Fig. 6. In general, for low-energy X-rays, both measured and analytical DEFs increased with increasing the thicknesses of GNF. However, the 6 MV FFF. beam even having a relative large amount of low-energy X-rays due to no filter failed to show any radioenhancement, i.e., the experimental and analytical results shown in Fig. 6 and Table 3 indicated that the dose enhancement by high-energy X-rays was negligible. The measured DEFs for 50 kVp were higher than the corresponding values for 220 kVp (Fig. 6(a) and 6(b)), regardless of the thicknesses of GNF, which was somewhat expected by the fact that photoelectric cross-sections steeply increase with decreasing photon energy. The analytical estimations of DEFs for the 220 kVp, and 6 MV FFF X-ray energies were in fair agreement within the error bars of measured data for all thicknesses of GNFs.

The microscopic dose enhancement was also calculated by replacing t_{RCF} = 25 μm in Eqs. (9) and (11) with the range of PEs in the active layer of RCF, $(\Re_{CSDA})_{T_o,RCF}$ = 4.0 μm for 50 kVp and $(\Re_{CSDA})_{T_o,RCF}$ = 19.5 μm for 220 kVp. Furthermore, by replacing it with the range of Auger electrons in the active layer of RCF, $(\Re_{CSDA})_{T_{ex},RCF}$ for 50 and 220 kVp, the microscopic dose enhancement up to these nanometer ranges was calculated. The results are summarized in Table 4.

4. Discussion

Numerous authors reported on dose enhancement by metal NPs. Most of them were based on MC simulations except for only a few on physical experimental observations and analytical calculations [6–21]. In all these approaches, the authors used different concentrations and sizes of GNPs, different X-rays energies, and experimental scenarios. Therefore, the exact one-to-one comparison with ours was nearly impossible. Cho *et al.* predicted a DEF of 1.92 for 50 kVp X-rays beam at a tumor loaded uniformly with 18 mg Au/g [11]. Roeske *et al.* calculated the dose enhancement from NPs of different atomic numbers at various energies by using the mass energy absorption coefficients [21]. Regulla *et al.* and Rakowski *et al.* adopted the similar method to determine DEFs [15,52]. Regulla *et al.* used a 150 μm-thick gold foil and thermally simulated exoelectron emission (TSEE) detector [52]. Their measured physical DEF was 100 within a range of 10 μm from the foil for 40 kVp

Table 4
Analytical microscopic dose enhancement factors (DEF) when the thickness of the active layer of radiochromic film (RCF), t_{RCF} is assumed to be equal to the ranges of photoelectrons, $(\Re_{CSDA})_{PE,RCF}$, and Auger electrons, $(\Re_{CSDA})_{AE,RCF}$.

GNF Thickness (nm)	50 kVp X-rays				220 kVp X-rays			
	$(\Re_{CSDA})_{PE,RCF}$(μm)	DEF	$(\Re_{CSDA})_{AE,RCF}$(nm)	DEF	$(\Re_{CSDA})_{PE,RCF}$(μm)	DEF	$(\Re_{CSDA})_{AE,RCF}$(nm)	DEF
20	4.0	4.1	524	7.0	19.5	1.9	674	4.1
30	4.0	5.9	499	10.7	19.5	2.4	651	5.9
40	4.0	7.5	478	14.2	19.5	2.9	629	7.8
50	4.0	9.2	456	17.9	19.5	3.4	608	9.7
100	4.0	16.9	350	38.2	19.5	5.8	506	19.9

X-rays. Rakowski *et al.* used GNFs and unlaminated EBT2 RCF to determine DEFs, as well as the MC method [15]. They showed a MC-calculated DEF of 19.31 within the first 0.25 μm-depth in water from 23 nm-thick GNF. However, their measured DEF using EBT2 for 50 kVp X-rays and a 23 nm-thick GNF was 1.29. Our analytical calculations for 50 kVp X-rays and a 20 nm-thick GNF suggest a DEF greater than 1.5. The underestimated DEF calculated by Rakowski *et al.* could be attributed to energy dependence of EBT2 film at low-energy X-rays [15].

Use of EBT-XD film in this study significantly reduced the disadvantage of dosimeter energy dependence, especially at low-energies. For 6 MV FFF X-rays, our measured and calculated DEFs were comparable to the previously published data (Fig. 6 and Table 3). For high-energy X-rays, Cho examined a dose enhancement for a concentration of 7 mg Au/g tumor using BEAMnrc/DOSXYZnrc and found a DEF of 1.014 [53]. Similarly, the DEF calculated by Roeske *et al.* was 1.01 [21]. Since low-energy X-rays have relatively high radioenhancement, superficial tumors could be one of potential candidates for the direct therapeutic application of GNPs or GNF.

The analytical calculations in the previous studies did not consider the dose contributions of Auger electrons and fluorescence X-rays [21,42]. In this work, we improved the analytical calculations by considering doses from Auger electrons and fluorescence X-rays separately. Our calculations show that the dose contribution by fluorescence X-rays generated in GNF was negligible whereas that by Auger electron was quite significant (> ~15%). However, CSDA ranges of AEs suggested that they deposit kinetic energy within the first few 100 nm in the active layer of RCF from the GNF-RCF interface. The doses measured by an optical scanner and Raman spectroscopy were averaged over the entire thickness of active layer of RCF. Therefore, comparison with the analytical DEF was made macroscopically. However, the calculated macroscopic DEF was smaller than the experimental results, especially at 50 kVp. The underestimation in analytical macroscopic DEFs may be in part due to not accounting for physical and chemical processes such as Plasmon decay, charge transfer, generation of LEEs from successive Compton scattering events followed by photoelectric effect, recombination and diffusion, and backscattering at the interface of low and high Z-material [6,21,42]. In addition, the NIST photon interaction data used for our analytical calculations was likely to be less accurate than the data implemented in the PENELOPE Monte Carlo system [54,55].

However, the calculated microscopic DEF within the ranges of photoelectrons and Auger electrons was extremely higher than the macroscopic values. This led to introducing the concept of microscopic dose enhancement within the range of these LEEs emitted by GNF, not in the entire thickness of the active layer of RCF (i.e., 25 μm). As expected, the microscopic dose enhancement within the range of Auger electrons was 7.0 to 38.2 for 50 kVp and 4.1 to 19.9 and 220 kVp with increase in GNF thicknesses from 20 to 100 nm. In addition, due to the short range of PEs especially by 50 kVp, the microscopic dose enhancement within the range of these electrons was even 2.7 to 4.7 times higher than the macroscopic dose enhancement over the entire active layer of RCF with increase in GNF thicknesses from 20 to 100 nm.

In our experiments GNF was in contact with the active layer of RCF. Under this condition, a fraction of the secondary electrons produced by X-rays should be backward due to their angular distribution as described in Fig. 2 [42,45]. The greater the X-rays energy, the lesser the fraction of backward secondary electrons. Therefore, the dosimetric model based on GNF has some limitations when compared to uniformly distributed GNPs through tissues. While considering GNF as an aggregation of GNPs in the proximity of tumor vasculatures or tumor cell membrane, the gold concentrations of both models would be different. Moreover, a large number of secondary electrons produced by X-rays can be bounced back to the air in the GNF-based model of this study.

5. Conclusions

The radioenhancement of 50, 220 kVp, and 6 MV X-rays with GNFs of 20 nm to 100 nm thickness was quantitatively validated by measuring the variations in optical densities and Raman spectra of RCF. In general, radioenhancement increases with increasing the thickness of GNF, while it decreases with increasing the energy of X-rays. The radioenehancement within the ranges of PEs and AEs emitted from gold was much higher than one estimated in the entire thickness of the target (e.g., cell, active layer of RCF). These experimental and analytical approaches developed in this study could quantitatively estimate radioenhancement by high-Z metallic NPs. However, due to a short range of LEEs emitted from gold, microscopic radioenhancement within the submicro range would be particularly important in a cell. In addition, the estimated DEFs of GNF in RCF may differ from those of GNP in tissues because of the difference in slow-down and scattering mechanism of LEEs.

Declaration of Competing Interest

The authors declare that they have no known competing financial interests or personal relationships that could have appeared to influence the work reported in this paper.

Acknowledgements

This work was in part supported by the National Research Foundation of Korea (NRF-2013M2B2B1075772 and NRF-2011-0018980) grants and the Nuclear Safety and Security Commission of Korea (490-2015036) grant.

Appendix A. Supplementary data

Supplementary data to this article can be found online at https://doi.org/10.1016/j.ejmp.2019.10.040.

References

[1] King RB, McMahon SJ, Hyland, et al. An overview of current practice in external beam radiation oncology with consideration to potential benefits and challenges for nanotechnology. Cancer Nanotechnol 2017:8.
[2] Wang AZ, Tepper JE. Nanotechnology in radiation oncology. J Clin Oncol 2014;32:2879–85.

[3] Farokhzad OC, Langer R. Nanomedicine: developing smarter therapeutic and diagnostic modalities. Adv Drug Deliv Rev 2006;58:1456–9.
[4] Jain KK. Applications of nanobiotechnology in clinical diagnostics. Clin Chem 2007;53:2002–9.
[5] Jung S, Sung W, Ye S-J. Pinhole X-ray fluorescence imaging of gadolinium and gold nanoparticles using polychromatic X-rays: a Monte Carlo study. Int J Nanomed 2017;12:5805–17.
[6] Kuncic Z, Lacombe S. Nanoparticle radioenhancement: principles, progress and application to cancer treatment. Phys Med Biol 2018;63.
[7] McMahon SJ, McNamara AL, Schuemann J, et al. Mitochondria as a target for radiosensitisation by gold nanoparticles. J Phys: Conf Ser; 2017. p. 777.
[8] Hainfeld JF, Slatkin JN, Smilowitz HM. The use of gold nanoparticles to enhance radiotherapy in mice. Phys Med Biol 2004;49:N309–15.
[9] McMahon SJ, Mendenhall MH, Jain S, et al. Radiotherapy in the presence of contrast agents: a general figure of merit and its application to gold nanoparticles. Phys Med Biol 2008;5:5635–51.
[10] Brun E, Sanche L, Roselli CS. Parameters governing gold nanoparticle X-ray radiosensitization of DNA in solution. Collo Surf B: Biointer 2009;72:128–34.
[11] Cho SH, Jones BL, Krishnan S. The dosimetric feasibility of gold nanoparticle-aided radiation therapy (GNRT) via brachytherapy using low-energy gamma-/x-ray sources. Phys Med Biol 2009;54:4889–905.
[12] Butterworth KT, McMahon SJ, Currell FJ, et al. Physical basis and biological mechanisms of gold nanoparticle radiosensitization. Nanoscale 2012;4:4830–8.
[13] Sung W, Ye S-J, McNamara AL, et al. Dependence of gold nanoparticle radiosensitization on cell geometry. Nanoscale 2017;9:5843–53.
[14] Delorme R, Taupin F, Flaender M, et al. Comparison of gadolinium nanoparticles and molecular contrast agents for radiation therapy-enhancement. Med. Phys. 2017;44:5949–60.
[15] Rakowski JT, Laha SS, Snyder MG, et al. Measurement of gold nanofilm dose enhancement using unlaminated radiochromic film. Med Phys 2015;42:5937–44.
[16] Nikjoo H, Lindborg L. RBE of low-energy electrons and photons. Phys Med Biol 2010;55:R65–109.
[17] Schuemann J, Berbeco R, Chithrani DB, et al. Roadmap to clinical use of gold nanoparticles for radiation sensitization. Int J Radiat Oncol Biol Phys 2016;94:189–205.
[18] Jones BL, Krishnan S, Cho SH. Estimation of microscopic dose enhancement factor around gold nanoparticles by Monte Carlo calculations. Med Phys 2010;37:3809–16.
[19] McMahon SJ, Butterworth KT, McGarry CK, et al. A computational model of cellular response to modulated radiation fields. Int J Radiat Oncol Biol Phys 2012;84:250–6.
[20] Lin Y, McMahon SJ, Paganetti H, et al. Biological modeling of gold nanoparticle enhanced radiotherapy for proton therapy. Phys Med Biol 2015;60:4149–68.
[21] Roeske JC, Nuñez L, Hoggarth M, et al. Characterization of the theorectical radiation dose enhancement from nanoparticles. Technol Canc Res Treat 2007;6:395–401.
[22] Palpant B, Prével B, Lermé J, et al. Optical properties of gold clusters in the size range 2–4 nm. Phys Rev B 1998;57:1963–70.
[23] Lewis DF, Chan MF. On GAFChromic EBT-XD film and the lateral response artifact. Med Phys 2016;43:643–9.
[24] Brown TA, Hogstrom KR, Alvarez D, et al. Dose-response curve of EBT, EBT2, and EBT3 radiochromic films to synchrotron-produced monochromatic x-ray beams. Med Phys 2012;39:7412–7.
[25] Crosbie JC, Svalbe I, Midgley SM, et al. A method of dosimetry for synchrotron microbeam radiation therapy using radiochromic films of different sensitivity. Phys Med Biol 2008;53:6861–77.
[26] Mirza JA, Park H, Park S-Y, et al. Use of radiochromic film as a high-spatial resolution dosimeter by Raman spectroscopy. Med Phys 2016;43:4520–8.
[27] Gafchromic™ EBT-XD Dosimetry film, Ashland Specialty Ingredients, Bridgewater, NJ 08807, 2015 http://www.gafchromic.com/documents/EBTXD_Specifications_Final.pdf.
[28] Palmer AL, Dimitriadis A, Nisbet A, et al. Evaluation of Gafchromic EBT-XD film, with comparison to EBT3 film, and application in high dose radiotherapy verification. Phys Med Biol 2015;60:8741–52.
[29] Menegotti L, Delana A, Martignano A. Radiochromic film dosimetry with flatbed scanners: a fast and accurate method for dose calibrationand uniformity correction with single film exposure. Med Phys 2008;35:3078–85.
[30] Saur S, Fengen J. GafChromic EBT film dosimetry with flatbed CCDscanner: a novel background correction method and full dose uncertaintyanalysis. Med Phys 2008;35:3094–101.
[31] Abramoff M, Magalhaes P, Ram S. Image processing with ImageJ. Biophotonics Int 2004;11:36–42.
[32] Pradeep T. A textbook of nanoscience and nanotechnology. New Delhi, India: Tata MacGraw-Hill; 2012. p. 846.
[33] Edwards HGM, Johnson AF, Lewis IR. Applications of Raman spectroscopy to the study of polymers and polymerization processes. J Raman Spectro 1993;24:475–83.
[34] Callens M, Crijns W, Simons V, et al. A spectroscopic study of the chromatic properties of Gafchromic™ EBT3 films. Med Phys 2016;43:1156–66.
[35] Price RL, Jerome WG. Basic confocal microscopy. New York, NY: Springer; 2011. p. 140.
[36] Gouadec G, Bellot-Gurlet L, Baron D, et al. Raman mapping for the investigation of nano-phased materials. In: Zoubir Arnaud, editor. Raman Imaging: Techniques and Applications. Berlin Heidelberg, Germany: Springer; 2012. p. 85–118.
[37] Raimondo C, Alloisio M, Demartini A, et al. Photopolymerization in water of diacetylenes chemisorbed onto noble metal nanoparticles: a spectroscopic study. J Raman Spectro 2009;40:1831–7.
[38] Ferraro JR, Nakamoto K, Brown CW. 2003. Introductory Raman Spectroscopy, 2nd ed. San Diego, CA: Elsevier Science, pp. 267, 274.
[39] Attix FH. Introduction to radiological physics and radiation dosimetry. Wiley-VCH Verlag GmbH & Co. KGaA, Weinheim 2008:p. 70, 156.
[40] Ngwa W, Makrigiorgos GM, Berbeco RI. Applying gold nanoparticles as tumor-vascular disrupting agents during brachytherapy: estimation of endothelial dose enhancement. Phys Med Biol 2010;55:6533–48.
[41] Hossain M, Su M. Nanoparticle location and material-dependent dose enhancement in X-ray radiation therapy. J Phys Chem 2012;116:23047–52.
[42] Paro AD, Hossain M, Webster TJ, et al. Monte Carlo and analytic simulations in nanoparticle-enhanced radiation therapy. Int J Nanomed 2016;11:4735–41.
[43] Williams GP. 2001. Electron binding energies. In: Thompson A C, Vaughan D, editors. X-ray data booklet, 2nd edition. Lawrence Berkeley National Laboratory.
[44] Goorley T, James M, Booth T, et al. Initial MCNP6 release overview. Nucl Technol 2012;180:298–315.
[45] Hunger H-J, Kuchler L. Measurements of the Electron Backscattering Coefficient for Quantitative EPMA in the Energy Range of 4 to 40 keV. Phys Stat Sol 1979;56:K45–8.
[46] Hubbell JH, Seltzer SM. Tables of x-ray mass attenuation coefficients and mass energy-absorption coefficients from 1 keV to 20 MeV for elements Z = 1 to 92 and 48 additional substances of dosimetric interest. Gaithersburg, MD: NISTIR-5632, National Institute of Standards and Technology; 1995.
[47] Berger MJ, Coursey JS, Zucker MA, et al. Stopping-Power & Range Tables for Electrons, Protons, and Helium Ions. Gaithersburg, MD: NISTIR-4999, National Institute of Standards and Technology; 1996.
[48] Scofield JH. Theoretical photoionization cross sections from 1 to 1500 keV. Livermore, CA: UCRL-51326, Lawrence Livermore National Laboratory; 1973.
[49] Hughes HG. Recent developments in low-energy electron/photon transport for MCNP6. Prog Nucl Sci Technol 2014;4:454–8.
[50] Siegel J, Lyutakov O, Rybka V, et al. Properties of gold nanostructures sputtered on glass. Nanoscale Res. Lett. 2011;6.
[51] Chauvenet W. A manual of spherical and practical astronomy. Philadelphia, PA: J. B. Lippincott & Co; 1871.
[52] Regulla DF, Hieber LB, Seidenbusch M. Physical and biological interface dose effects in tissue due to X-ray-induced release of secondary radiation from metallic gold surfaces. Radiat Res 1998;150:92–100.
[53] Cho SH. Estimation of tumour dose enhancement due to gold nanoparticles during typical radiation treatments: a preliminary Monte Carlo study. Phys Med Biol 2005;50:N163–73.
[54] Salvat F. 2014. PENELOPE-2014: A code system for Monte Carlo simulation of electron and photon transport. Report NEA/NSC/DOC 2014.
[55] Seltzer SM, Fernández-Varea JM, Andreo P, Bergstrom PM, Burns DT, Bronić IK, et al. Key data for ionizing-radiation dosimetry: measurement standards and applications. ICRU Report 90 2016.